Corrosion Science 255 (2025) 113116

Contents lists available at ScienceDirect

Corrosion Science

journal homepage: www.elsevier.com/locate/corsci

Temperature-dependent oxidation behavior of Y-Hf co-doped and Co-free $Al_{16}Cr_{20}Fe_{20}Ni_{44}$ eutectic multi-principal elements alloy at 1100–1300 °C

Aihui Huang [a,b], Yusheng Tian [a,b], Yifeng Tang [a,b], Guoliang Zhu [a,b,*], Shilin Xia [a], Xiaofeng Zhao [b], Paul K. Chu [d], Chao Yang [c,**], Xiaoqin Zeng [c]

[a] Suzhou Laboratory, Suzhou 215000, China
[b] Shanghai Key Laboratory of Advanced High-Temperature Materials and Precision Forming, School of Materials Science and Engineering, Shanghai Jiao Tong University, Shanghai 200240, China
[c] National Engineering Research Center of Light Alloy Net Forming, Shanghai Jiao Tong University, Shanghai 200240, China
[d] Department of Physics, Department of Materials Science & Engineering, and Department of Biomedical Engineering, City University of Hong Kong, Tat Chee Avenue, Kowloon 999077, Hong Kong

ARTICLE INFO

Keywords:
High-temperature oxidation
High-entropy alloy
Eutectic Structure

ABSTRACT

Eutectic multi-principal elements alloys (EMPEAs) are promising candidates for high-temperature applications due to their exceptional mechanical properties and thermal stability. Herein, the temperature-dependent oxidation behavior of a Y-Hf co-doped Co-free $Al_{16}Cr_{20}Fe_{20}Ni_{44}$ EMPEA in the temperature range between 1100 and 1300 °C is investigated. The oxidation product is exclusively Al_2O_3 scale with the columnar grain microstructure in this temperature range, indicating that inward O diffusion plays a more critical role than Al diffusion, consequently leading to a small oxidation rate. At 1100–1200 °C, the EMPEA exhibits superior oxidation resistance due to the higher Al activity and lower reactive element (RE) in the Al-depleted layer, while the smaller coefficient of thermal expansion (CTE) minimizes residual stress. However, the EMPEA shows inferior oxidation resistance at 1300 °C, likely because the inherent softness degrades the interfacial instability under elevated thermal stress, leading to oxide scale spallation. All in all, the Y-Hf co-doped Co-free $Al_{16}Cr_{20}Fe_{20}Ni_{44}$ EMPEA has large potential in high-temperature applications and offers a cost-effective alternative with sustained performance stability up to 1200 °C.

1. Introduction

Multi-principal elements alloys (MPEAs) composed of four or more principal elements in near-equal or varying concentrations have garnered significant attention due to their unique design principle and properties, including mechanical strength, thermal stability, and corrosion resistance [1–5]. However, single-phase MPEAs with face-centered cubic (FCC) or body-centered cubic (BCC) structures suffer from the inherent trade-off between strength and ductility, and either insufficient yield strength or poor plastic deformation underscores the need for alternative alloy designs. In response to this challenge, researchers have explored dual-phase MPEAs, particularly those incorporating aluminum. Al-containing dual-phase MPEAs show a combination of strength and ductility, which is often attributed to their composite microstructures consisting of soft and hard phases. For instance, alloys such as AlCrFeCoNiNb and AlTiFeCoNi exhibit hardness values exceeding 1000 Hv [6,7], while compositions like $Al_{0.1}$CoCrFeNi have demonstrated excellent corrosion resistance in aggressive environments [8]. These properties make Al-containing MPEAs promising candidates for structural and functional applications under harsh service conditions.

Building upon this dual-phase concept, eutectic high-entropy alloys (EMPEAs) have been introduced by Lu et al. to balance strength and ductility [9]. EMPEAs are typically composed of a fine and stable eutectic microstructure with a soft phase (FCC) with good ductility and a hard phase (BCC or other intermetallic compound) with high strength. The eutectic nature of EMPEAs also produces excellent high-temperature stability, tensile strength, and creep resistance [10–12], as the different phases mitigate phase transformation or decomposition under thermal stress.

* Corresponding author at: Suzhou Laboratory, Suzhou 215000, China.
** Corresponding author.
E-mail addresses: glzhu@sjtu.edu.cn (G. Zhu), chaoyang0315@163.com (C. Yang).

https://doi.org/10.1016/j.corsci.2025.113116
Received 12 April 2025; Received in revised form 7 June 2025; Accepted 14 June 2025
Available online 16 June 2025

In high-temperature applications involving turbine engines and aerospace components [13,14], it is essential to investigate the oxidation behavior of EMPEAs. Previous studies on the oxidation behavior of EMPEAs have mainly focused on the formation mechanism and growth of oxide scales [15–21]. These studies suggest that the oxidation resistance of EMPEAs can be enhanced by adding refractory elements [15,16], the incorporation of Al, Cr, and Si to promote the formation of protective oxide scales [17–19], controlling the heat treatment [20], optimizing the composition [21–23], and doping with reactive elements (REs) [24–27]. In particular, doping with REs is an effective approach to improve oxide scale adhesion and reduce the growth of oxide scale on metallic alloys [28,29]. For instance, Y-Hf co-doped AlCoCrFeNi-type EMPEAs have been shown to have good oxidation resistance at 1100–1300 °C [25–27]. However, research on the oxidation behavior of RE-doped EMPEAs in other systems has been limited.

Furthermore, cobalt (Co), an essential element in many EMPEA systems, has raised practical concerns due to resource availability, high cost and potential radioactivity [30,31]. As a result, there is a growing urgency to develop Co-free EMPEAs that retain the desired mechanical and high-temperature properties while addressing the challenge associated with Co. Iron (Fe), as a more abundant and cost-effective alternative to Co, offers a potentially promising solution. Moreover, Fe is known to bring additional benefits to the oxidation resistance of NiAl alloys or coatings by promoting the formation of protective α-Al_2O_3 scales [32,33]. Despite these advantages, systematic investigations into Fe-substituted, Co-free EMPEAs are limited, particularly regarding their oxidation behavior at elevated temperatures. The Co-free $Al_{16}Cr_{20}Fe_{20}Ni_{44}$ EMPEA has excellent mechanical properties at room temperature (ultimate tensile strength of ~1 GPa and total elongation of ~12 %) [34], which represents a promising candidate. However, to the best of our knowledge, its oxidation behavior, especially with RE-doping, remains unreported.

In this study, we investigate the oxidation behavior of a Co-free $Al_{16}Cr_{20}Fe_{20}Ni_{44}$ EMPEA in the temperature range between 1100 °C and 1300 °C. The EMPEA is doped with REs (Y and Hf) to improve oxide scale adhesion. Three different temperatures are selected to evaluate the effects of temperature on the oxidation behavior of the alloy. The microstructures of the pristine alloy, oxidized alloy, and oxide scale are characterized in detail to gain a comprehensive understanding of the oxidation mechanism. The results enrich our knowledge on the oxidation resistance of cost-effective Co-free AlCrFeNi-type EMPEAs in high-temperature applications.

2. Materials and methods

2.1. Materials preparation and isothermal oxidation

Two $Al_{16}Cr_{20}Fe_{20}Ni_{44}$ EMPEA ingots, each weighing approximately 100 g, were prepared by adding Y and Hf (0.025 at% each). The alloys were melted in a Ti-gettered, high-purity argon atmosphere and used high purity metals (>99.9 wt%) to minimize contamination. The ingots were remelted five times to achieve microstructural homogeneity. Table 1 shows the chemical composition of the EMPEAs, determined using inductively coupled plasma optical emission spectroscopy (ICP-OES).

The square plates (10 × 10 × 2.5 mm) were cut from the ingot by a precision cutting machine (Accutom 5, Struers), ground with 5000-grit SiC paper, and cleaned in an ultrasonic bath for 5 min. The isothermal oxidation tests were conducted at 1100 °C, 1200 °C, and 1300 °C, in a muffle furnace for up to 500 h. The maximum oxidation time at 1300 °C was limited to 100 h to prevent severe degradation. After the chamber furnace reached the target temperature, the specimens were uniformly positioned at the center of the furnace to ensure consistent thermal exposure and reproducible oxidation conditions. After heating for the pre-set time, the specimens were removed from the furnace and air-cooled for 10 min with the help of a fan.

Table 1
Composition of the Y-Hf co-doped $Al_{16}Cr_{20}Fe_{20}Ni_{44}$ EMPEA determined by inductively-coupled plasma optical emission spectrometry (ICP-OES) experiment.

Elements						
	Al	Cr	Fe	Ni	Y	Hf
wt%	8.34	20.08	21.57	49.88	0.038	0.082
at%	16.2	19.9	19.8	44.1	0.025	0.027

2.2. Characterization

The phase structure of pristine and oxidized alloys was determined by X-ray diffraction (XRD, Bruker D8 ADVANCE) with Cu Kα radiation (λ = 1.5406 Å, generated at 40 kV and 10 mA) at a scanning rate of 5°/min and 2θ scanning range of 10°-90°. Microstructural and compositional analyses of the alloys and oxide scales were conducted by scanning electron microscopy (SEM, Mira3, Tescan) with an accelerating voltage of 20 kV, energy-dispersive X-ray spectroscopy (EDS, Oxford Instruments), and electron backscattering diffraction (EBSD, Oxford Instruments NordlysMax3) with an accelerating voltage of 20 kV. The surface chemical states were determined by X-ray photoelectron spectroscopy (XPS, Thermo Fisher, ESCALAB 250X).

To protect the cross-sectional samples during analysis, a layer of Ni was electroplated onto the oxide scales. The electroplating solution consists of a mixture of $NiSO_4{\cdot}6\ H_2O$ (200 g/L), $NiCl_2{\cdot}6\ H_2O$ (50 g/L) and H_3BO_3 (20 g/L), with a solution pH of 4.0–4.5. The current density is 100 mA/cm^2, and the electroplating time is 5 min. The average coefficient of thermal expansion (CTE) was determined using a high-temperature dilatometer (DIL 402 Expedis Select/Supreme, NETZSCH, Germany) in argon between 25 °C and 1250 °C at a MPEAting rate of 5 °C/min. The specimens for the CTE measurements were rectangular with dimensions of 15 × 3 × 2.5 mm. The residual stress in the oxide scales was measured by photoluminescence piezospectroscopy (PLPS) on a confocal Raman microprobe (LabRAM HR, Horiba Jobin Yvon, France) equipped with a 532 nm Nd:YAG laser. The residual stress (σ) was calculated by Eq. (1) [35]:

$$\Delta\nu = 5.07\sigma \tag{1}$$

where $\Delta\nu$ is the peak shift of the R2 line with respect to that of the stress-free sapphire. The spectra were analyzed by the mixed Gaussian-Lorentzian functions (Labspec software) to determine the peak positions, and PLPS was employed to monitor the phase transformation of Al_2O_3 during the early stage of alloy oxidation.

3. Results

3.1. Microstructure of $Al_{16}Cr_{20}Fe_{20}Ni_{44}$ EMPEA

Fig. 1 shows the microstructure of $Al_{16}Cr_{20}Fe_{20}Ni_{44}$ EMPEA. According to the BSE analysis (Fig. 1a-b), the alloy has a dual-phase eutectic structure consisting of bright and dark phases. XRD confirms that the eutectic microstructure comprises γ'/γ and A2/β phases (Fig. 1c). Based on the morphology of the eutectic microstructure, two distinct regions are identified: lamellar and rod-like eutectic structures. BSE-EDS mapping indicates that the bright phase is enriched with Cr and Fe, while the dark phase is enriched with Al and Ni (Fig. 1d-g). The thickness of each phase in the lamellar structure ranges from 0.5 to 1 μm, and the size of the rod-like eutectic microstructure is between 1 and 2 μm.

Moreover, EBSD characterization is performed to provide a more comprehensive understanding of the microstructure, revealing an average grain size of approximately 25 μm and a random grain orientation without apparent crystallographic texture (Fig. 2a-b). Further

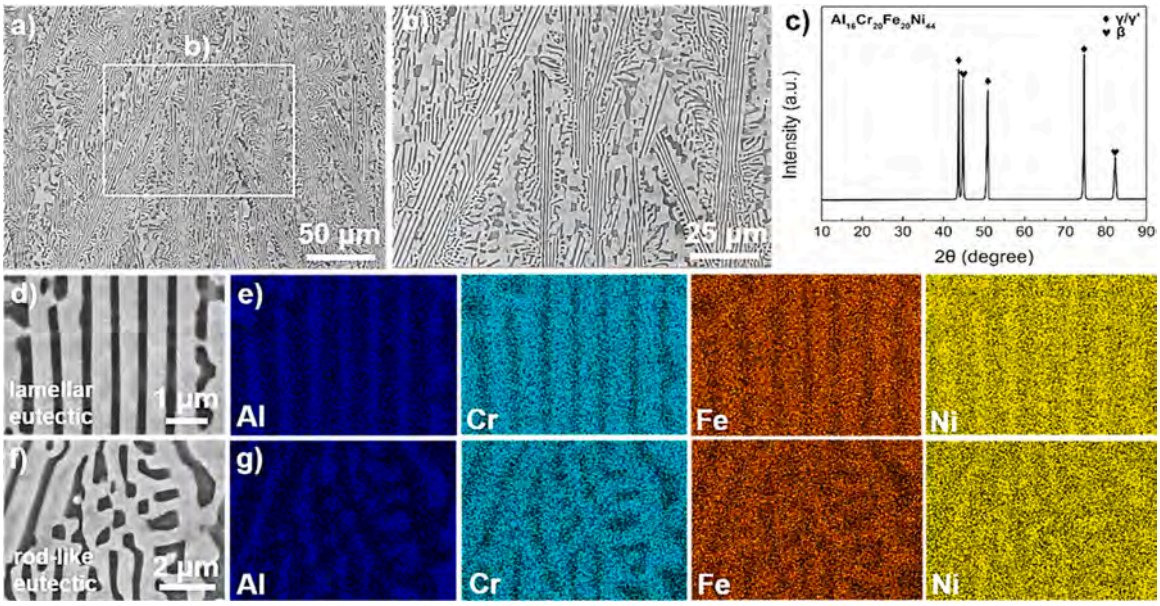

Fig. 1. Microstructure of Y-Hf co-doped $Al_{16}Cr_{20}Fe_{20}Ni_{44}$ EMPEA: (a and b) Low and High-magnification BSE images, showing the overview of microstructure; (c) XRD spectrum; (d-e) BSE image and EDS elemental maps, showing the lamellar eutectic microstructure; (f-g) BSE image and EDS elemental maps, showing the rod-like eutectic microstructure.

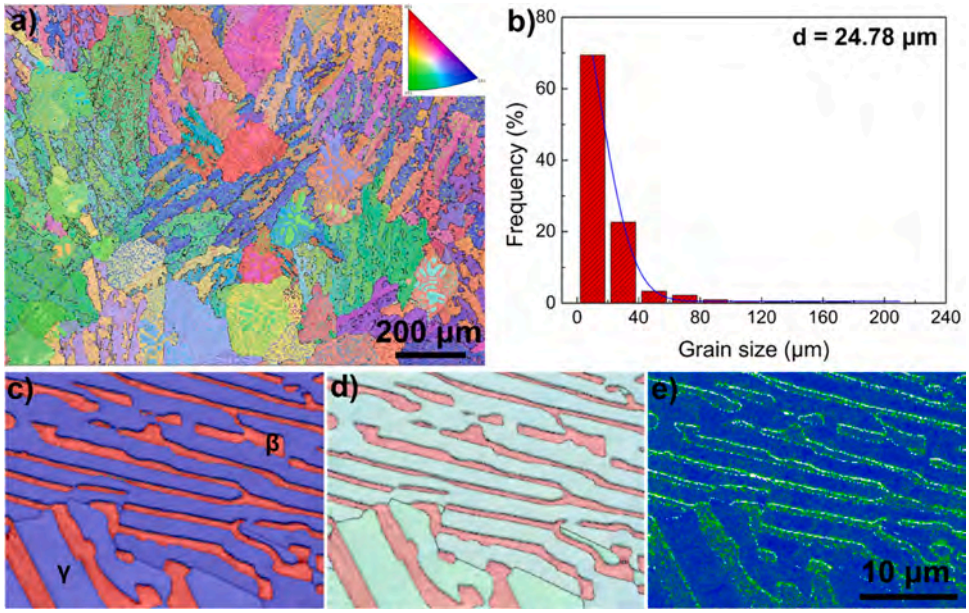

Fig. 2. EBSD analysis of Y-Hf co-doped $Al_{16}Cr_{20}Fe_{20}Ni_{44}$ EMPEA: (a) Misorientation map, showing the overall grain morphology; (b) Grain size distribution histogram providing quantitative assessment of grain size; (c-f) Phase map, misorientation map and kernel average misorientation map collectively illustrating the characteristic eutectic microstructure.

analysis verifies that the bright phase corresponds to the FCC phase, whereas the dark phase is the BCC phase (Fig. 2c-d). Kernel average misorientation (KAM) mapping indicates that local strain is primarily concentrated within the BCC phase (Fig. 2e), which can be attributed to its higher hardness than FCC phase. According to the TEM analysis from the prior study [34], the BCC phase exhibits an ordered B2 structure, whereas the FCC phase is characterized as disordered. Table 2 presents the chemical compositions of the γ and β phases determined by EDS, which reveals no Y- or Hf-precipitates due to the small concentration (0.025 at%).

Table 2
Chemical composition of the γ and β phases of Y-Hf co-doped $Al_{16}Cr_{20}Fe_{20}Ni_{44}$ EMPEA by BSE-EDS experimental point analysis (Error bar derived from 5 points).

Elements	Phases	
	γ phase (at%)	β phase (at%)
Al	11.7 ± 1.3	31.7 ± 2.3
Cr	24.7 ± 1.5	9.9 ± 0.9
Fe	22.6 ± 1.5	13.1 ± 1.3
Ni	41.0 ± 1.2	47.4 ± 2.1

3.2. Oxidation behavior of $Al_{16}Cr_{20}Fe_{20}Ni_{44}$ EMPEA at 1100–1300 °C

To investigate the initial oxidation behavior of the Y-Hf co-doped $Al_{16}Cr_{20}Fe_{20}Ni_{44}$ EMPEA, the surface morphology and phase composition were analyzed after 5 min oxidation at 1100 °C (Fig. 3). Low-magnification and high-magnification SEM images (Fig. 3a-c) reveal the oxide morphology, with larger grain size of Al_2O_3. PLPS and XPS analysis confirm the exclusive formation of α-Al_2O_3 (Fig. 3d and Fig. S2), with no detectable θ-Al_2O_3. This indicates a rapid θ- to α-Al_2O_3 phase transformation in Y-Hf co-doped $Al_{16}Cr_{20}Fe_{20}Ni_{44}$ EMPEA, which will be discussed in Section 4.1.

Fig. 4 shows the surface and cross-sectional morphologies of Y-Hf co-doped $Al_{16}Cr_{20}Fe_{20}Ni_{44}$ EMPEA after 500 h oxidation at 1100 °C. As shown in Fig. 4a, the oxide scale remains intact without spallation. The Y- and Hf-rich oxides are distributed predominantly along the grain boundaries of the oxide scale (Fig. 4b-c), consistent with the dynamic segregation theory [36]. XRD and XPS analysis confirm that the primary oxidation product is α-Al_2O_3 (Fig. 4d and Fig. S1). BSE-EDS mapping further reveals good adhesion between the α-Al_2O_3 scale and $Al_{16}Cr_{20}Fe_{20}Ni_{44}$ EMPEA substrate without interfacial imperfections such as pores (Fig. 4e-g). The microstructure of the underlying alloy exhibits a coarser dual-phase eutectic morphology after oxidation for 500 h. The thickness of the α-Al_2O_3 scale and Al-depleted layer are about 3.5 μm and 20 μm.

After oxidation for 500 h at 1200 °C, the surface and cross-sectional morphologies of the Y-Hf co-doped $Al_{16}Cr_{20}Fe_{20}Ni_{44}$ EMPEA are shown in Fig. 5. Consistent with the results at 1100 °C, no spallation is observed from the oxide scale surface (Fig. 5a). Nevertheless, the uniformity of the oxide scale decreases at 1200 °C, with more pronounced agglomeration of Y- and Hf-rich oxides along the grain boundaries (Fig. 5b-d) because of accelerated diffusion of reactive elements at the higher temperature. According to our previous work [27], these Y- and Hf-rich oxides are identified as $HfY_xAl_yO_{2+3/2(x+y)}$ with a monoclinic crystal structure (Hf: 23.5, Y: 7.9; Al: 8.3; O: 60.3 in at%). XRD, XPS analysis and BSE-EDS mapping (Fig. 5e-h and Fig. S1) indicate that α-Al_2O_3 is the primary oxidation product, and the interface between the oxide scale and substrate remains intact without showing visible pores or cracks. Prolonged exposure at 1200 °C also results in significant coarsening of the dual-phase eutectic microstructure of the alloy substrate (Fig. 5f). It should be noted that the oxide scale thickness increases significantly to approximately 6.8 μm, accompanied by a thicker Al-depleted layer with a thickness of about 40 μm (Fig. 5g).

EBSD analysis further reveals that the α-Al_2O_3 scale grows preferentially along the close-packed directions of the substrate phases (Fig. S6). Specifically, the [0001] direction of α-Al_2O_3 is aligned with the [111] direction of the γ phase and the [110] direction of the β phase, indicating a strong orientation relationship governed by crystallographic coherency. This suggests that the oxide preferentially nucleates and grows along the close-packed planes of the underlying substrate, which helps minimize interfacial energy and promotes the formation of dense, adherent oxide scales.

For comparison, the oxidation behavior of the Y-Hf co-doped $Al_{16}Cr_{20}Fe_{20}Ni_{44}$ EMPEA is compared with that of the Y-Hf co-doped $Al_{18}Co_{20}Cr_{20}Ni_{42}$ EMPEA in which Fe is replaced by Co. These alloys have nearly the same Al, Cr and Ni concentrations, making them well-suited for isolating the effects of Fe versus Co on the oxidation behavior. After oxidation for 250 h at 1200 °C, the Co-containing $Al_{18}Co_{20}Cr_{20}Ni_{42}$ EMPEA shows significant spallation zones on the oxide scale surface (Fig. 6a-b) together with oxide intrusions surrounding Y/Hf-rich oxide in the spallation areas (Fig. 6c). Cross-sectional analysis reveals interfacial imperfections (pores and oxide intrusions) and Al_2O_3 as the oxidation product (Fig. 6d-f). In contrast, the Fe-containing $Al_{16}Cr_{20}Fe_{20}Ni_{44}$ EMPEA has no interfacial impurities on the oxidized surface or in the cross-section after oxidation for 500 h at 1200 °C (Fig. 5), thus corroborating the superior oxidation resistance.

Unlike the oxidation results at 1100 °C and 1200 °C, pronounced spallation occurs on the oxide scale after oxidation for 100 h at 1300 °C exposing the substrate partially (Fig. 7a). Moreover, interfacial rumpling is found from the surface of the oxide scale (Fig. 7b). BSE images and EDS mapping (Fig. 7c-e) reveal that Y/Hf-rich oxides, which are

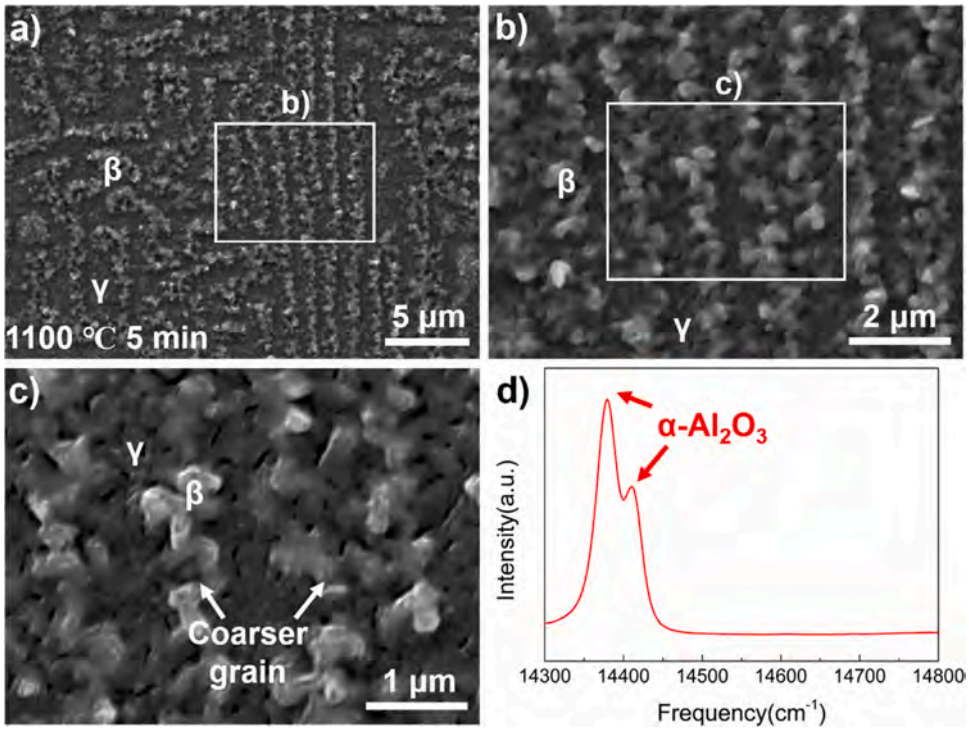

Fig. 3. Surface morphology and PLPS analysis of Y-Hf co-doped $Al_{16}Cr_{20}Fe_{20}Ni_{44}$ EMPEA after 5 min oxidation at 1100 °C: (a) Low-magnification SE images showing the oxidized surface; (b and c) High-magnification SE images revealing the detailed morphology of the oxidized surface formed on the γ and β phases; (d) PLPS spectrum confirming the exclusive formation of α-Al_2O_3.

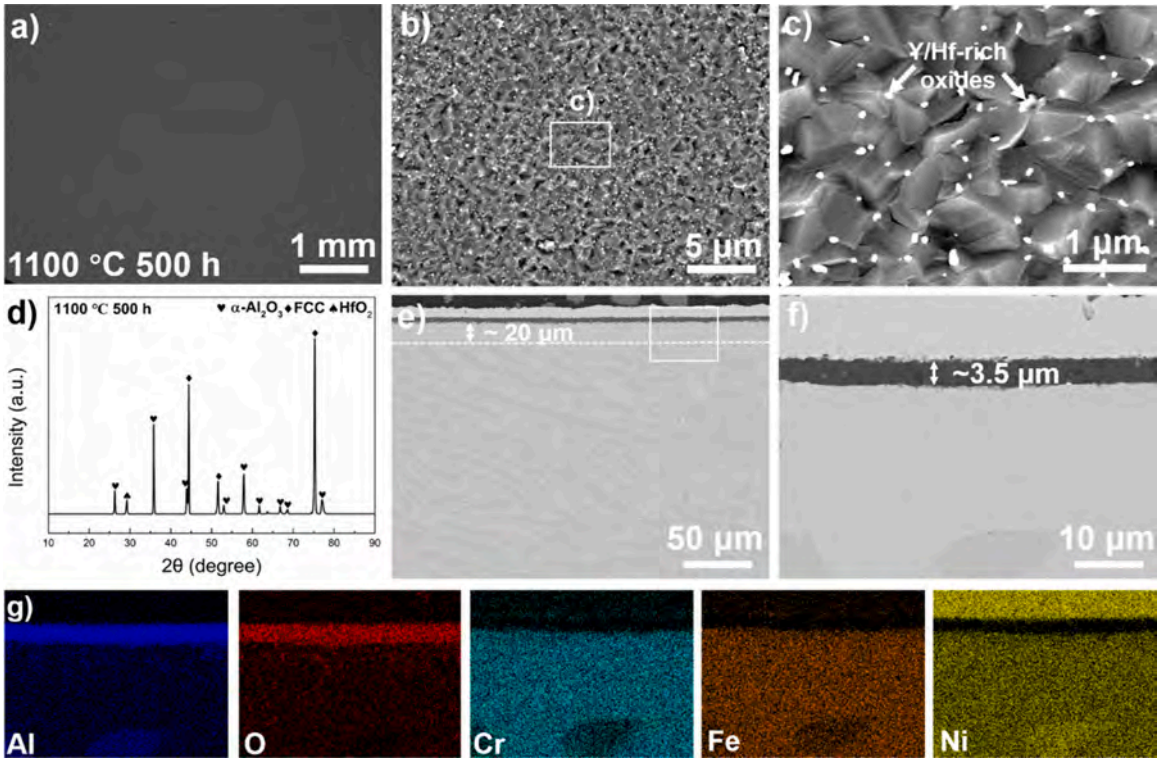

Fig. 4. Surface and cross-sectional morphologies of Y-Hf co-doped $Al_{16}Cr_{20}Fe_{20}Ni_{44}$ EMPEA after 500 h oxidation at 1100 °C: (a) Low-magnification BSE image of the intact oxide scale; (b and c) High-magnification BSE images showing the detailed surface morphology of the oxide scale; (d) XRD spectrum; (e) Low-magnification BSE image of the adherent oxide scale; (f) High-magnification BSE image and (g) EDS elemental maps of the oxidation product.

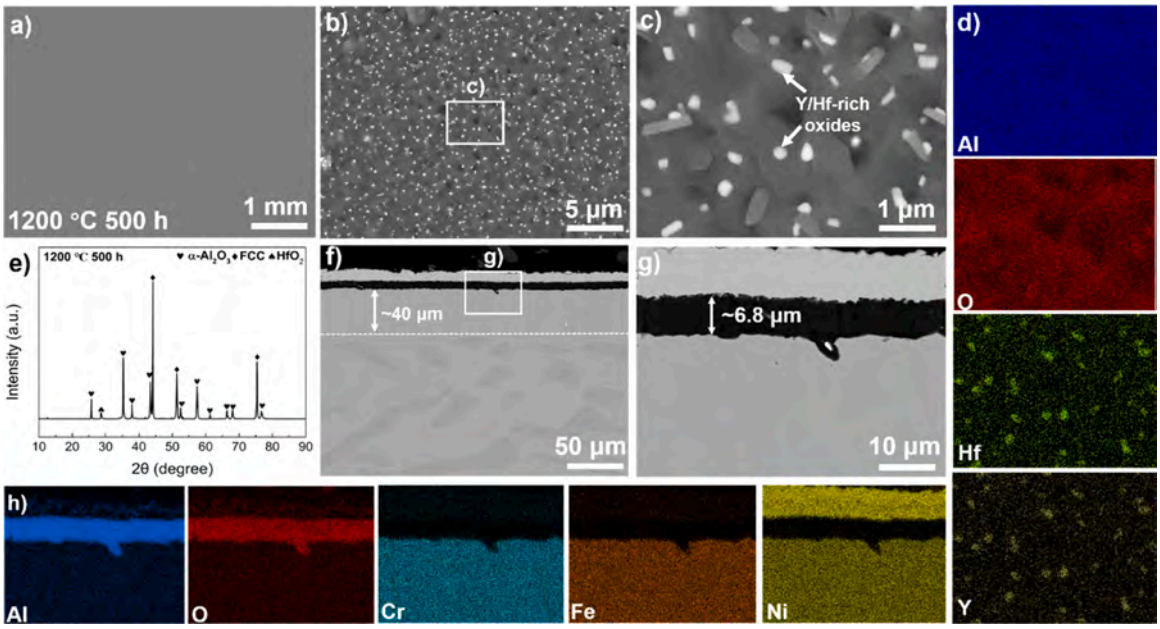

Fig. 5. Surface and cross-sectional morphologies of Y-Hf co-doped $Al_{16}Cr_{20}Fe_{20}Ni_{44}$ EMPEA after 500 h oxidation at 1200 °C: (a) Low-magnification BSE image of the intact oxide scale; (b and c) High-magnification BSE images and (d) EDS elemental maps showing the detailed morphology of the Y/Hf-rich oxide along the grain boundaries of the oxide scale; (e) XRD spectrum showing the phase structure after oxidation; (f) Low-magnification BSE image of the adherent oxide scale; (g) High-magnification BSE image and (h) EDS elemental maps of the oxidation product.

distributed along grain boundaries, increase in size compared to lower-temperature oxidation. These larger oxide particles arise from the larger diffusion rates of reactive elements and localized coalescence at this temperature. XRD confirms that α-Al_2O_3 remains the primary oxidation product after oxidation at 1300 °C (Fig. 7f). Cross-sectional BSE-EDS analysis further verifies interfacial rumpling and partial detachment (Fig. 7g-h). Nonetheless, despite these negative effects, the remaining oxide scale has a thickness of approximately 10 μm, while the Al-depleted layer extends to about 55 μm. These findings reveal the accelerated oxidation kinetics and greater challenge in maintaining

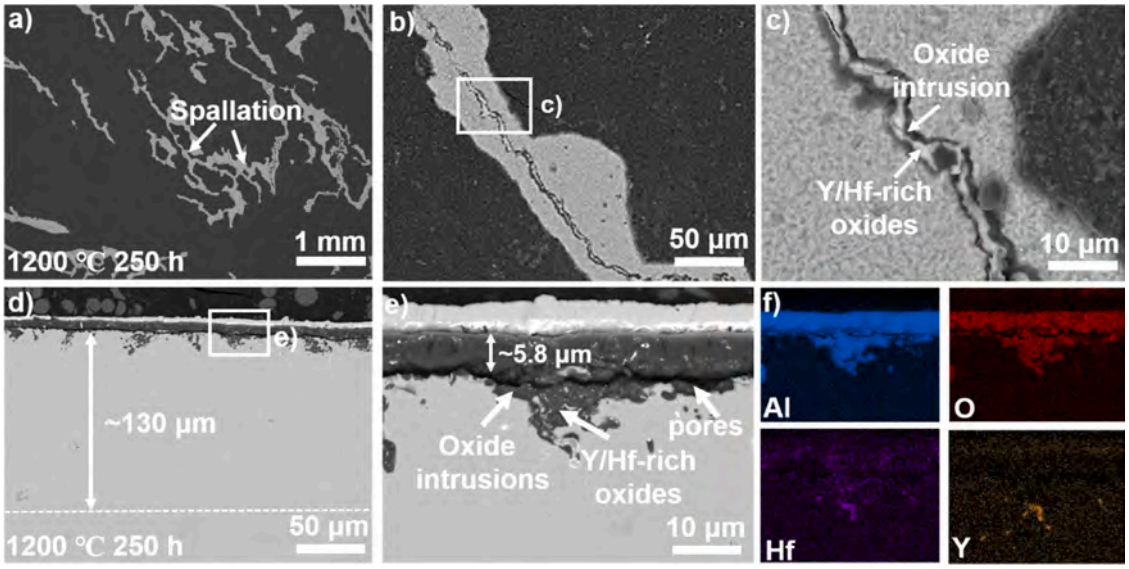

Fig. 6. Surface and cross-sectional morphologies of Y-Hf co-doped $Al_{18}Co_{20}Cr_{20}Ni_{42}$ EMPEA after 250 h oxidation at 1200 °C: (a) Low-magnification BSE image showing the oxide scale; (b and c) High-magnification BSE images revealing the detailed spallation zone; (d) Low-magnification BSE image showing the cross-sectional morphology; (g) High-magnification BSE image and (h) Corresponding EDS elemental maps revealing the oxidation product and oxide intrusions.

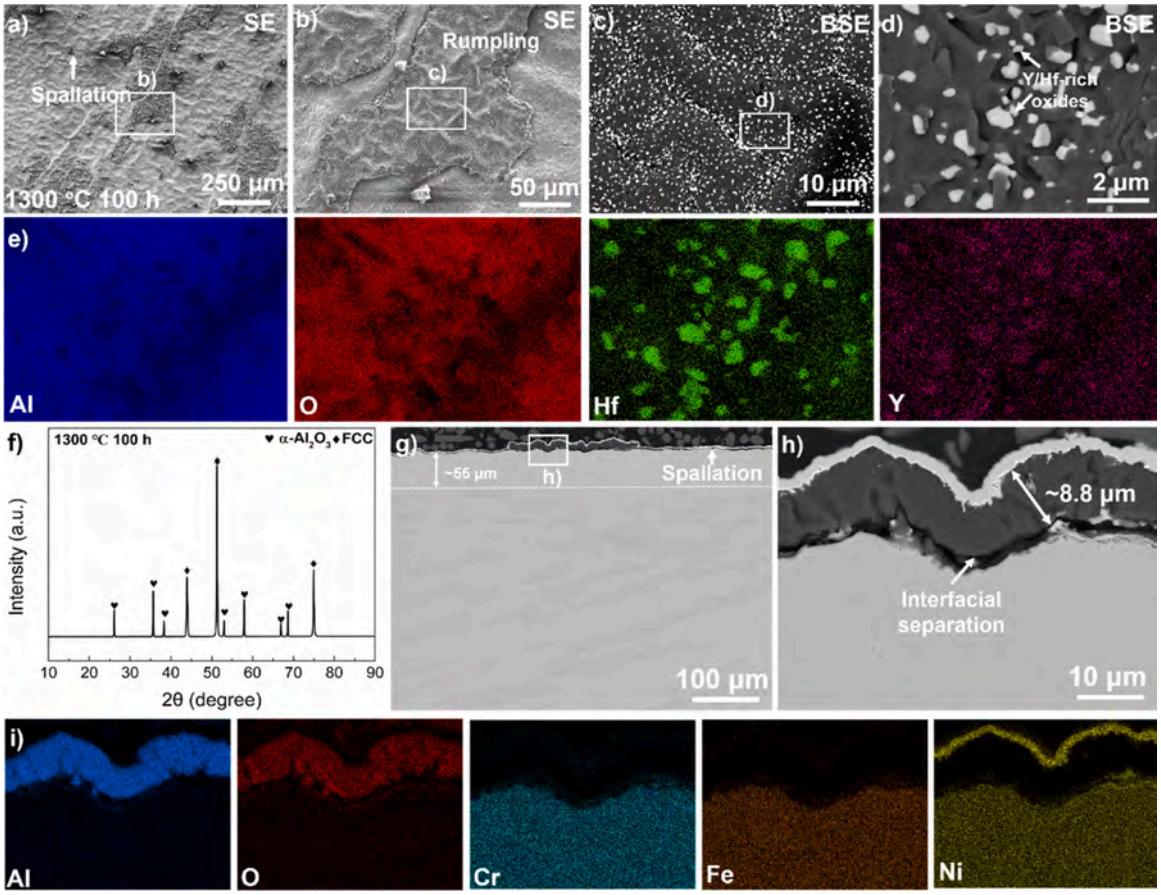

Fig. 7. Surface and cross-sectional morphologies of Y-Hf co-doped $Al_{16}Cr_{20}Fe_{20}Ni_{44}$ EMPEA after 100 h oxidation at 1300 °C: (a-b) Low and high-magnification SE image showing spallation and rumpling of the oxide scale; (c-d) High-magnification BSE images and (e) EDS elemental maps showing the detailed morphology of the Y/Hf-rich oxide; (f) XRD pattern revealing the phase structure after oxidation; (g) Low-magnification BSE image of the cross-sectional oxide scale; (h) High-magnification BSE image and (i) EDS maps of the oxidation product.

scale adhesion at 1300 °C.

3.3. Microstructure of oxide scales at 1100–1300 °C

Fig. 8a-c shows the fractured cross-sectional microstructures of the oxide scales formed on the Y-Hf co-doped $Al_{16}Cr_{20}Fe_{20}Ni_{44}$ EMPEA after oxidation for 500 h at 1100–1200 °C and 100 h at 1300 °C. All the oxide scales show the typical double-layer structure comprising outer equiaxed grains and inner columnar grains. The outer equiaxed grains remain notably thin (300–400 nm) and show little variation in thickness despite the increasing oxidation temperature. This means that the inner columnar grain structure dominates the oxide scale, and the growth is primarily driven by inward oxygen diffusion [37,38]. Quantitative analysis of the oxide grains (Fig. 8d-i) reveals that the average width of columnar grains increases significantly from ~0.8 μm to ~1.9 μm with rising temperature. This is likely due to enhanced oxygen diffusion as well as coarsening and lateral expansion of the columnar grain structure in the oxide scale.

3.4. Oxidation kinetics of $Al_{16}Cr_{20}Fe_{20}Ni_{44}$ EMPEA at 1100–1300 °C

Based on the results in Figs. 3–6, Al_2O_3 is the predominant oxidation product on the Y-Hf co-doped $Al_{16}Cr_{20}Fe_{20}Ni_{44}$ EMPEA between 1100 °C and 1300 °C. As the growth of Al_2O_3 scales is controlled by diffusion, the oxidation rate of Y-Hf co-doped $Al_{16}Cr_{20}Fe_{20}Ni_{44}$ EMPEA at 1100–1300 °C can be calculated based on the Al_2O_3 scale thickness by the classical Wagner's theory [39] :

$$h_t = (k_h t)^{1/2} \tag{2}$$

where h_t is the scale thickness after an oxidation time t and k_h is the parabolic rate constant obtained by linear fitting of the scale thickness to the square root of oxidation time, as shown in Fig. 9. To facilitate the direct comparison of the parabolic rate constants with those of conventional Al_2O_3 -forming alloys, the parabolic rate constant in cm^2/s can be converted to the unit g cm^{-4} s^{-1} by the following relationship [40]:

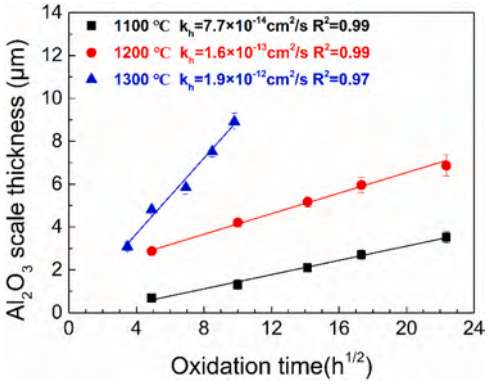

Fig. 9. Alumina scale thickness versus the square root of oxidation time at 1100–1300 °C with the alumina scale thickness evaluated based on a minimum of 50 measurements taken from 5 distinct cross-sectional BSE images.

$$k_p = \left(\frac{3M_O\rho_{Al_2O_3}}{M_{Al_2O_3}}\right)^2 k_h \tag{3}$$

where k_p represents the parabolic rate constant in g cm^{-4} s^{-1}. The parameters used in this calculation are the molar masses of Al_2O_3 (102 g/mol) and oxygen (16 g/mol) and the density of Al_2O_3 (3.98 g/cm^3). The parabolic rate constants k_p are calculated to be $2.7 \pm 0.1 \times 10^{-13}$ g^2 cm^{-4} s^{-1}, $9.8 \pm 0.3 \times 10^{-13}$ g^2 cm^{-4} s^{-1} and $6.0 \pm 0.2 \times 10^{-12}$ g^2 cm^{-4} s^{-1} at 1100 °C, 1200 °C and 1300 °C, respectively.

To evaluate the oxidation kinetics of the Y-Hf co-doped $Al_{16}Cr_{20}Fe_{20}Ni_{44}$ EMPEA, mass gain measurements were performed at 1100 °C and 1200 °C. The mass gain per unit area (Δm/S) exhibits a linear

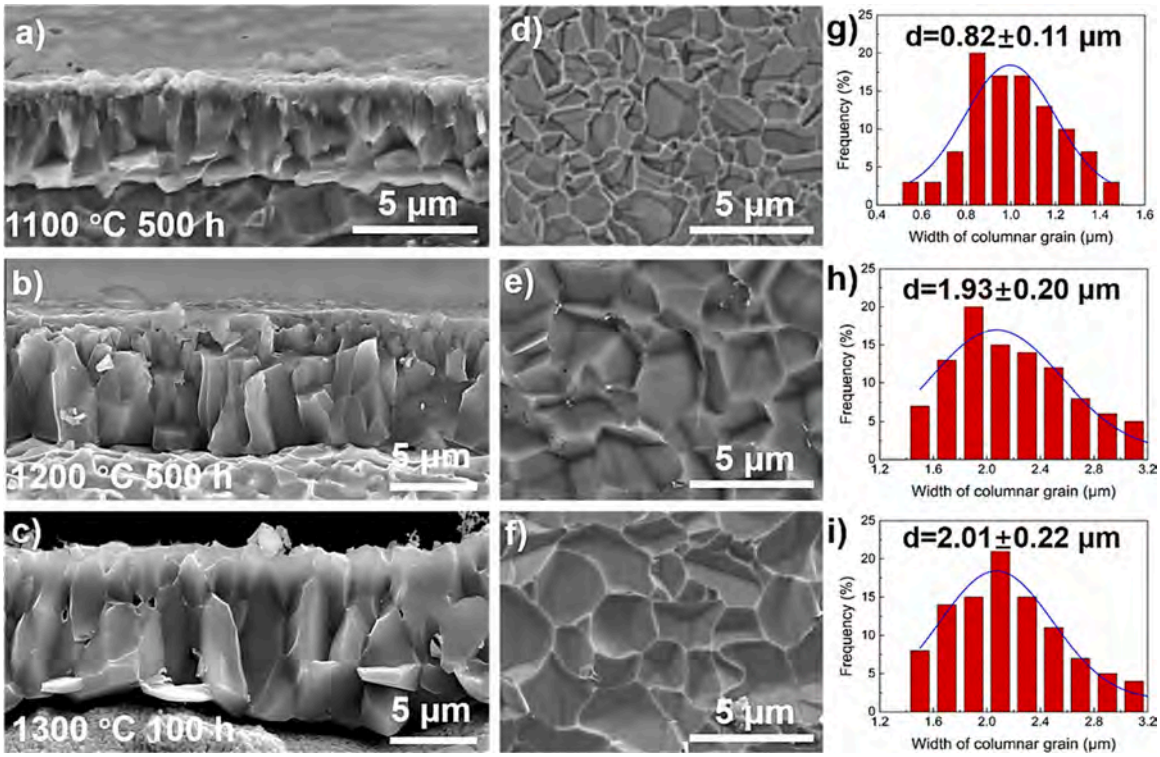

Fig. 8. Microstructural analysis of the oxide scales on Y-Hf co-doped $Al_{16}Cr_{20}Fe_{20}Ni_{44}$ EMPEA after 500 h oxidation at 1100–1200 °C and 100 h oxidation at 1300 °C: (a-c) Fractured cross-sectional microstructures of the oxide scales; (d-f) Columnar α-Al_2O_3 grains left on the substrates; (g-i) Widths of columnar grains based on at least 50 grains in each alloy). The fractured cross-sectional microstructures of the oxide scales are obtained by mechanical fracturing.

relationship with the square root of oxidation time ($t^{0.5}$), indicating that the oxidation behavior follows a parabolic rate law (Fig. S4). This suggests the formation of a continuous, slow-growing, and adherent oxide scale. The corresponding parabolic rate constants (k_P), determined using the equation $\Delta m^2/S^2 = k_P \cdot t$, are 2.98×10^{-13} $g^2 \cdot cm^{-4} \cdot s^{-1}$ at 1100 °C and 1.04×10^{-12} $g^2 \cdot cm^{-4} \cdot s^{-1}$ at 1200 °C. These values are in good agreement with the rate constants independently extracted from oxide scale thickness measurements (2.7×10^{-13} and 9.8×10^{-13} $g^2 \cdot cm^{-4} \cdot s^{-1}$, respectively), thereby validating the consistency of the oxidation model. At 1300 °C, severe spallation of the oxide scale occurs during long-term exposure, which introduces significant uncertainty in mass gain data. Therefore, the k_P value at this temperature is only estimated based on cross-sectional scale thickness. While this approach provides an approximate indication of oxidation rate, it may not fully capture transient kinetic behavior or early-stage deviations from diffusion-controlled growth. Further work need be required to validate the kinetic trends at such high temperatures.

Table 3 compares the oxidation rates of various EMPEAs with the same RE dopant concentrations and conventional oxidation-resistant alloys at 1100–1300 °C. The $Al_{16}Cr_{20}Fe_{20}Ni_{44}$ EMPEA shows a slightly higher oxidation rate than the lightly Co-containing $AlCoCrFeNi_{2.1}$ EMPEA but shows a slower oxidation rate than the high Co concentration $Al_{18}Co_{20}Cr_{20}Ni_{42}$ and $Al_{18}Co_{30}Cr_{10}Fe_{10}Ni_{32}$ EMPEAs. Moreover, the $Al_{16}Cr_{20}Fe_{20}Ni_{44}$ EMPEA completely eliminates the use of the expensive element, Co, consequently reducing the material costs while maintaining excellent oxidation resistance. It should be noted that the oxidation rate constant of $Al_{16}Cr_{20}Fe_{20}Ni_{44}$ EMPEA is significantly lower than that of conventional oxidation-resistant FeCrAlY(Hf) alloys. Although its oxidation rate is slightly inferior to that of NiAl(Hf), the latter suffers from intrinsic brittleness [41], which severely limits its applicability in structural components. Meanwhile, the interface between the Al_2O_3 scale and $Al_{16}Cr_{20}Fe_{20}Ni_{44}$ EMPEA remains intact even after oxidation for 500 h at 1200 °C, in contrast to the spalled and rumpling interfaces in conventional NiAl, FeCrAlY and NiCoCrAlY(Hf) alloys [42–44]. In summary, the cost-effective Y-Hf co-doped $Al_{16}Cr_{20}Fe_{20}Ni_{44}$ EMPEA shows excellent oxidation resistance at high temperature.

4. Discussion

The cost-effective Co-free $Al_{16}Cr_{20}Fe_{20}Ni_{44}$ EMPEA, doped with Y and Hf, exhibits good oxidation resistance between 1100 and 1200 °C, with performance comparable to that of some Co-containing EMPEAs (Table 3), as evidenced by stable oxide scale formation and adhesion.

Table 3
Comparison of k_p of the Y-Hf co-doped $Al_{16}Cr_{20}Fe_{20}Ni_{44}$ EMPEA with those of other Al_2O_3-forming EMPEAs at 1100 °C and 1200 °C [25–27,29,45,46].

Temperature (°C)	EMPEAs	k_p (g^2 cm^{-4} s^{-1})	Reference
1100	(Y-Hf) $Al_{16}Cr_{20}Fe_{20}Ni_{44}$	$2.7 \pm 0.1 \times 10^{-13}$	This work
/	(Y-Hf) $Al_{18}Co_{20}Cr_{20}Ni_{42}$	4.6×10^{-13}	[45]
/	(Y-Hf) $Al_{18}Co_{30}Cr_{10}Fe_{10}Ni_{32}$	2.9×10^{-13}	[25]
/	(Y-Hf) $AlCoCrFeNi_{2.1}$	2.1×10^{-13}	[26]
/	(Y-Hf) FeCrAl	3.7×10^{-13}	[29]
/	NiAlHf	1.6×10^{-13}	[46]
1200	(Y-Hf) $Al_{16}Cr_{20}Fe_{20}Ni_{44}$	$9.8 \pm 0.3 \times 10^{-13}$	This work
/	(Y-Hf) $Al_{18}Co_{30}Cr_{10}Fe_{10}Ni_{32}$	1.3×10^{-12}	[25]
/	(Y-Hf) $AlCoCrFeNi_{2.1}$	9.5×10^{-13}	[26]
/	(Y-Hf) FeCrAl	3.5×10^{-12}	[29]
/	NiAlHf	7.6×10^{-13}	[46]
1300	(Y-Hf) $Al_{16}Cr_{20}Fe_{20}Ni_{44}$	$6.0 \pm 0.2 \times 10^{-12}$	This work
/	(Y-Hf) $Al_{18}Co_{30}Cr_{10}Fe_{10}Ni_{32}$	6.3×10^{-12}	[25]
/	(Y-Hf) $AlCoCrFeNi_{2.1}$	2.3×10^{-11}	[27]
/	(Y-Hf) FeCrAl	2.2×10^{-11}	[29]

However, interfacial rumpling and spallation are observed after oxidation for 100 h at 1300 °C, indicating worsening oxidation resistance at higher temperatures. These findings suggest that the oxidation resistance is governed by both the alloy composition and oxidation temperature. Therefore, the following discussion focuses on the effects of Fe and temperature on the oxidation resistance of Y-Hf co-doped $Al_{16}Cr_{20}Fe_{20}Ni_{44}$ EMPEA.

4.1. Effects of Fe on the early oxidation characteristics of Y-Hf co-doped $Al_{16}Cr_{20}Fe_{20}Ni_{44}$ EMPEA

During oxidation below 1200 °C, metastable θ-Al_2O_3 forms initially on conventional NiCoCrAlY and NiAlHf alloys or coatings and transforms into more stable α-Al_2O_3 scales with time [47,48]. Since the growth rate of θ-Al_2O_3 is higher than that of α-Al_2O_3, it is necessary to understand the θ- to α-Al_2O_3 transformation. Generally, the phase transformation time varies from a few minutes to hours depending on the composition and grain size of the alloy or coating and oxidation temperature [49,50]. In our study, SEM and PLPS analysis are performed to study the role of Fe in the alloy after oxidation for 5 min at 1100 °C (Fig. 4). No θ-Al_2O_3 is detected on the oxidized surface of the β and γ phases, in contrast to the $Al_{18}Co_{20}Cr_{20}Ni_{42}$ EMPEA in which θ-Al_2O_3 constitutes ~3.5 wt% of the Al_2O_3 scale [45]. This suggests that Fe promotes the θ- to α-Al_2O_3 phase transformation, possibly due to the initial formation of α-Fe_2O_3 with the same crystal structure as α-Al_2O_3 [51]. In the Co-containing EMPEA, the formation of Co oxides, such as CoO (face-centered cubic structure) or Co_3O_4 (cubic structure), may delay the θ- to α-Al_2O_3 phase transformation, as their crystal structures are more similar to that of θ-Al_2O_3 (cubic) than α-Al_2O_3 (corundum). This structural similarity may stabilize the transient θ-Al_2O_3 phase and hinder its transformation into the thermodynamically stable α-Al_2O_3.

The α-Al_2O_3 grain formed on the surface of the β phase is larger than that of the γ phase (Fig. 4**c**). It is generally accepted that the grain size of α-Al_2O_3 mainly depends on the phase composition, number of nucleation sites, and oxidation temperature [52]. Since the oxidation temperature is constant, the different grain sizes of these two phases arise from the phase composition and number of nucleation sites. It is well known that the number of nucleation sites is influenced by the conversion rate of θ-Al_2O_3 to α-Al_2O_3. According to the literature [53], the growth of θ-Al_2O_3 depends on the Al diffusion rate. The Al diffusion coefficients of the γ and β phases are calculated by the thermo-calc software based on the EDS result (Table 4). The Al diffusion coefficient of the β phase is larger than that of the γ phase, suggesting that faster Al diffusion in the β phase facilitates the growth and transformation of θ-Al_2O_3 to α-Al_2O_3. The rapid transformation reduces the number of nucleation sites, leading to fewer but larger α-Al_2O_3 grains on the β phase surface. Conversely, in the γ phase, slower Al diffusion restricts the growth of θ-Al_2O_3, resulting in a greater number of nucleation sites and smaller α-Al_2O_3 grains. These differences in the α-Al_2O_3 grain size highlight the significant role of Al diffusion in the microstructural evolution during oxidation.

4.2. Effects of Fe on the oxidation resistance of Y-Hf co-doped $Al_{16}Cr_{20}Fe_{20}Ni_{44}$ EMPEA

The oxidation behavior of the Y-Hf co-doped $Al_{18}Co_{20}Cr_{20}Ni_{42}$ EMPEA at 1200°C (see Fig. 9) shows significant spallation and interfacial imperfections, in contrast to the intact oxide scale of the Fe-

Table 4
Al diffusion coefficients of the γ and β phases at 1100 ℃ calculated by the Thermo-calc software using TCNI8 and TCHEA7 databases.

Database	D^{γ}_{Al} (cm^2/s)	D^{β}_{Al} (cm^2/s)
TCNI8	1.33×10^{-13}	7.30×10^{-11}
TCHEA7	1.34×10^{-13}	7.25×10^{-11}

containing $Al_{16}Cr_{20}Fe_{20}Ni_{44}$ EMPEA (Fig. 4). Based on the aforementioned results, the primary difference in the oxidation resistance of the two EMPEAs stems from oxide intrusion at the scale/EMPEA interface. It is predominantly influenced by the distribution of RE-rich oxides during oxidation, and the distribution depends on the RE solubility in the Al-depleted layer. To explore the effects of RE solubility, thermodynamic calculations are performed using the thermo-Calc software to calculate the solubility of Y and Hf in the γ and β phases of both alloys. However, the solubility of Y cannot be determined accurately on account of its strong tendency to form Ni-Y intermetallic compounds [54,55]. The solubility of Hf in the β phase in the Fe-containing $Al_{16}Cr_{20}Fe_{20}Ni_{44}$ EMPEA is about × 2 higher than that in the Co-containing $Al_{18}Co_{20}Cr_{20}Ni_{42}$ EMPEA, but about × 0.5 lower in the γ phase (Fig. 10 and Table 5). Since the Al-depleted layer is the γ phase, the higher RE solubility of the γ phase in the Co-containing $Al_{18}Co_{20}Cr_{20}Ni_{42}$ EMPEA contributes to the formation of interfacial impurities at 1200 °C.

The thickness of the Al-depleted layer increases with time due to the consumption of Al to form the Al_2O_3 scale. The process also promotes the formation of RE-rich oxides at the scale/alloy interface. According to Fig. 4 and Fig. 9, the thickness of the Al-depleted layer in $Al_{18}Co_{20}Cr_{20}Ni_{42}$ EMPEA (~130 μm thick after 250 h oxidation at 1200 °C) is larger than that of the $Al_{16}Cr_{20}Fe_{20}Ni_{44}$ EMPEA (only ~40 μm thick after 500 h oxidation at 1200 °C). Since the thickness of the Al-depleted layer is controlled by the Al activity, the Al activity of γ in these two EMPEAs is calculated (Table 6). The Al activity of the γ phase in $Al_{16}Cr_{20}Fe_{20}Ni_{44}$ EMPEA is higher than that of the $Al_{18}Co_{20}Cr_{20}Ni_{42}$ EMPEA by about 1.5 times. This implies that Fe enhances the Al activity in the γ phase and a thinner Al-depleted layer. Compared to the $Al_{18}Co_{20}Cr_{20}Ni_{42}$ EMPEA, the lower RE solubility and higher Al activity in the γ phase contribute to the superior oxidation resistance of the $Al_{16}Cr_{20}Fe_{20}Ni_{44}$ EMPEA.

The residual stress in the Al_2O_3 scale affects the oxidation resistance due to its impact on the elastic strain energy in the oxide scale. As shown in Fig. 11a, the residual stresses of the Al_2O_3 scale in $Al_{16}Cr_{20}Fe_{20}Ni_{44}$ are about −5.2 GPa and −6.4 GPa after oxidation at 1100 °C and 1200 °C, respectively, which are substantially lower than those of the Co-containing $Al_{18}Co_{20}Cr_{20}Ni_{42}$ EMPEA which shows compressive stresses of approximately −6.3 GPa and −7.4 GPa at the corresponding temperature. At room temperature, the residual stress in the oxide scale is governed by thermal mismatch stress arising from the differential coefficient of thermal expansion (CTE) between the alloy substrate and the Al_2O_3 scale [56]. This stress emerges during cooling as a result of the thermal contraction difference between the alloy and oxide scale. As shown in Fig. 11b, the CTE of $Al_{16}Cr_{20}Fe_{20}Ni_{44}$ EMPEA (17.0×10^{-6}/K) is less than that of $Al_{18}Co_{20}Cr_{20}Ni_{42}$ EMPEA (18.4×10^{-6}/K) at 1200 °C, suggesting that the residual stress in these two alloys is altered by the different CTE of the two alloys. According to the literature [57], β-phase alloys have a smaller CTE than γ-phase alloys at a high temperature.

Table 5
Hf solubility of the γ and β phases at 1200 °C calculated by the thermo-calc software using TCNI8 and TCHEA7 databases.

EMPEAs	Hf solubility in β phase	Hf solubility in γ phase
$Al_{18}Co_{20}Cr_{20}Ni_{42}$	0.036 at% (TCNI8)	0.017 at% (TCNI8)
$Al_{18}Co_{20}Cr_{20}Ni_{42}$	0.041 at% (TCHEA7)	0.018 at% (TCHEA7)
$Al_{16}Cr_{20}Fe_{20}Ni_{44}$	0.073 at% (TCNI8)	0.008 at% (TCNI8)
$Al_{16}Cr_{20}Fe_{20}Ni_{44}$	0.075 at% (TCHEA7)	0.006 at% (TCHEA7)

Table 6
Al activity of the γ phases at 1200 °C calculated by the thermo-calc software. $Al_{18}Co_{20}Cr_{20}Ni_{42}$ EMPEAs using TCNI8 and TCHEA7 databases.

EMPEAs	a^{γ}_{Al} (TCNI8)	a^{γ}_{Al} (TCHEA7)
$Al_{18}Co_{20}Cr_{20}Ni_{42}$	6.55×10^{-7}	6.27×10^{-7}
$Al_{16}Cr_{20}Fe_{20}Ni_{44}$	9.33×10^{-7}	1.07×10^{-6}

Table 7
Volume fraction and size of Y-Hf oxide particles at the Al_2O_3 grain boundaries after oxidation at 1100–1300 °C based on Image J analysis of the experimental results (The volume fraction and average size of Y-Hf oxide particles are determined by quantitative 10000 × and 30000 × BSE images).

Oxidation temperature and time	Volume fraction (%)	Average size (nm)
1100 °C 500 h	2.1 ± 0.7	160 ± 50
1200 °C 500 h	4.2 ± 1.2	310 ± 60
1300 °C 100 h	6.3 ± 2.1	750 ± 80

Since $Al_{16}Cr_{20}Fe_{20}Ni_{44}$ EMPEA (~41 %) has a considerably bigger volume fraction of the β phase than the $Al_{18}Co_{20}Cr_{20}Ni_{42}$ EMPEA (~31 %), the reduction in CTE can be ascribed to the higher volume fraction of the β phase.

4.3. Effects of temperature on the oxidation resistance of Y-Hf co-doped $Al_{16}Cr_{20}Fe_{20}Ni_{44}$ EMPEA

Interfacial rumpling and spallation are observed after oxidation for 100 h at 1300 °C, indicating worse oxidation resistance of Y-Hf co-doped $Al_{16}Cr_{20}Fe_{20}Ni_{44}$ EMPEA at the higher temperature. According to the dynamic segregation theory [36], RE ions diffuse outward along the oxide scale grain boundaries to form RE-rich oxides, which can lower the oxidation rate and enhance the scale plasticity. However, the diffusivity of RE ions increases rapidly with increasing temperature, especially above 1200 °C, leading to a larger volume fraction and average size of RE-rich oxide particles (Table 6). When RE ions diffuse more rapidly along the scale grain boundaries at 1300 °C, their effects on scale plasticity weaken. Consequently, scale adhesion becomes increasingly dependent on the mechanical properties of the alloy substrate.

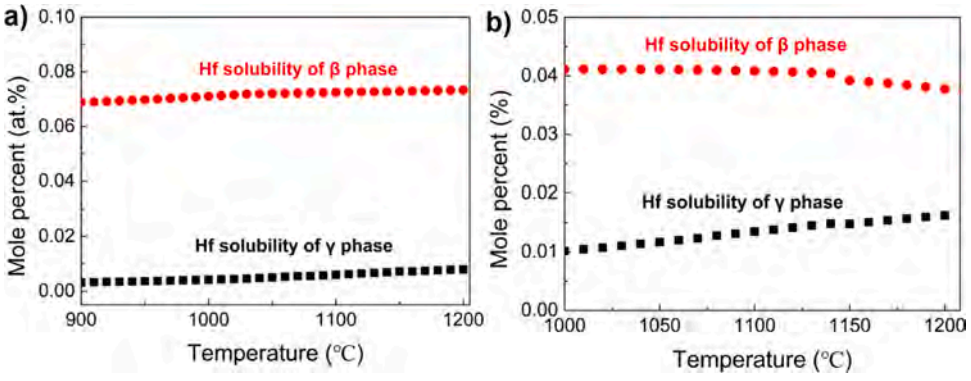

Fig. 10. Calculated Hf solubility of the β and γ phase sin (a) Y-Hf co-doped $Al_{16}Cr_{20}Fe_{20}Ni_{44}$ EMPEA and (b) Y-Hf co-doped $Al_{18}Co_{20}Cr_{20}Ni_{42}$ EMPEA at 900–1200 °C.

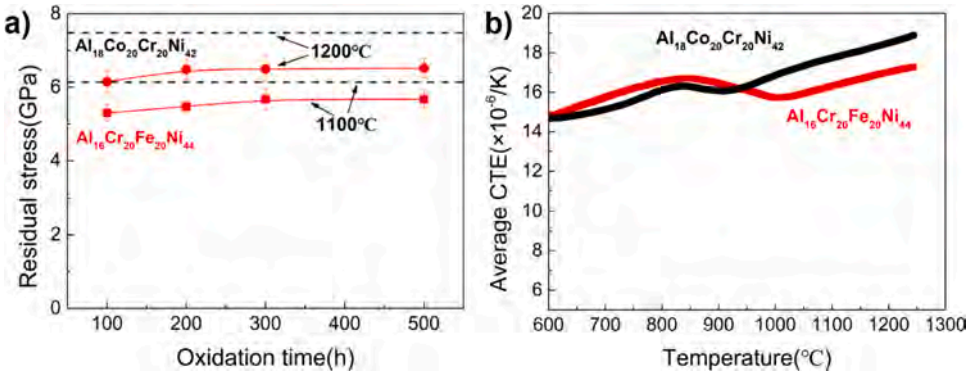

Fig. 11. (a) Residual stress in the Al_2O_3 scales on Y-Hf co-doped $Al_{16}Cr_{20}Fe_{20}Ni_{44}$ EMPEA after oxidation at 1100 °C and 1200 °C; (b) Evolution of the average CTE of Y-Hf co-doped $Al_{16}Cr_{20}Fe_{20}Ni_{44}$ EMPEA from 600 °C to 1250 °C.

Fe-containing MPEAs generally have lower hardness and yield strength than Co-containing MPEAs due to the strong solid-solution strengthening of Co [58,59]. We also measured the high-temperature compressive stress-strain curves of Y-Hf co-doped $Al_{16}Cr_{20}Fe_{20}Ni_{44}$ and $Al_{18}Co_{20}Cr_{20}Ni_{42}$ EMPEAs at 1300 °C for comparison (Fig. S5). The results show that the Y-Hf co-doped $Al_{16}Cr_{20}Fe_{20}Ni_{44}$ EMPEA exhibits significantly higher compressive strength of ~38 MPa, compared to ~24 MPa for the $Al_{18}Co_{20}Cr_{20}Ni_{42}$ counterpart (~24 MPa). Moreover, the Y-Hf co-doped $AlCoCrFeNi_{2.1}$ and $Al_{18}Co_{30}Cr_{10}Fe_{10}Ni_{32}$ EMPEAs shows excellent oxidation resistance at 1300 °C [25,27], as there is no spallation found on their oxidized surface after 100 h oxidation. Therefore, the inherent softness of the Fe-containing EMPEA may increase the susceptibility to interfacial mechanical failure and compromise the oxidation resistance at 1300 °C due to the interplay between diminished scale plasticity and the limited capacity of the alloy to accommodate deformation.

4.4. Oxidation mechanism of Y-Hf co-doped $Al_{16}Cr_{20}Fe_{20}Ni_{44}$ EMPEA

The oxidation behavior of the Y–Hf co-doped $Al_{16}Cr_{20}Fe_{20}Ni_{44}$ EMPEA is governed by a diffusion-controlled mechanism, as evidenced by the parabolic growth kinetics of the oxide scale observed at 1100–1300 °C (Fig. 7 and Table 3). The formation of a continuous and adherent α-Al_2O_3 scale serves as the key barrier against further oxidation. Fractured SEM and EBSD images (Fig. 6a-c and Fig. S6) reveal the predominant presence of columnar α-Al_2O_3 grains growing perpendicular to the substrate surface, which is indicative of inward oxygen diffusion being the dominant transport process during oxidation [36,37].

The Al element plays a key role in forming and stabilizing the protective α-Al_2O_3 scale. The high Al activity in this alloy facilitates rapid outward diffusion of Al to the oxide/alloy interface. This promotes the formation of thermodynamically stable α-Al_2O_3 at 1100–1200 °C, where the protective scale exhibits excellent adherence and structural integrity. The co-doping of Hf and Y, each at 0.025 at%, also plays a crucial role in enhancing scale adhesion and reducing oxidation rate. Both reactive elements segregate to grain boundaries and form discrete RE-rich oxide particles within the scale. This segregation behavior leads to improved oxide scale adhesion through the dynamic segregation effect and possibly by inhibiting void formation at the metal/oxide interface [28,60]. Furthermore, the relatively low solubility of Hf in the γ matrix phase (Table 5) helps to suppress excessive interfacial reaction zones or Kirkendall voids, thereby enhancing the mechanical stability of the oxide scale.

However, at elevated temperatures (e.g., 1300 °C), the formation of coarser RE-rich oxide particles within the scale and inherent softness of this alloy decrease the ability of the oxide to accommodate growth stresses plastically (Table 6 and Fig. S5). As a result, local spallation or rumpling is occasionally observed after long-term exposure. In summary, the superior oxidation resistance of the Y-Hf co-doped $Al_{16}Cr_{20}Fe_{20}Ni_{44}$ EMPEA arises from the synergistic contributions of fast and sufficient Al supply for protective α-Al_2O_3 formation and the scale-anchoring effect of reactive elements.

5. Conclusions

The oxidation behavior of Y-Hf co-doped Co-free $Al_{16}Cr_{20}Fe_{20}Ni_{44}$ EMPEA in the temperature range between 1100 °C and 1300 °C is investigated. The EMPEA shows better oxidation resistance than Y-Hf co-doped Co-containing $Al_{18}Co_{20}Cr_{20}Ni_{42}$ EMPEA at 1100–1200 °C. The enhanced oxidation resistance can be attributed to the higher Al activity, low RE solubility of the γ phase, and lower CTE. However, the EMPEA shows inferior oxidation resistance at 1300 °C possibility due to its inherent softness, which can degrade the interfacial instability under elevated thermal stress. The $Al_{16}Cr_{20}Fe_{20}Ni_{44}$ EMPEA has large potential in high-temperature applications due to its affordability and sustained stability and offers a cost-effective alternative with sustained stability up to 1200 °C.

Author statement

The authors claim that this manuscript neither in whole nor in part has been previously considered by this journal. And this manuscript in whole and in part has not been considered by another journal, and not involving plagiarism with copyright infringement issues. I hereby declare and guarantee those are true, I claimed.

CRediT authorship contribution statement

Aihui Huang: Writing – review & editing, Writing – original draft, Investigation, Formal analysis, Data curation, Conceptualization. **Xiaofeng Zhao:** Writing – review & editing, Methodology, Investigation. **Guoliang Zhu:** Writing – review & editing, Methodology, Investigation, Formal analysis, Conceptualization. **Yifeng Tang:** Visualization, Software, Methodology. **Yusheng Tian:** Validation, Resources, Investigation. **Shilin Xia:** Methodology, Software, Validation, Visualization. **Xiaoqin Zeng:** Writing – review & editing, Supervision, Formal analysis. **Chao Yang:** Writing – review & editing, Investigation, Funding acquisition, Conceptualization. **Paul K. Chu:** Writing – review & editing, Investigation, Funding acquisition.

Declaration of Competing Interest

The authors declare that they have no known competing financial interests or personal relationships that could have appeared to influence the work reported in this paper.

Acknowledgments

This work was financially supported by the Postdoctoral Fellowship Program of CPSF (No. GZC20231545), China Postdoctoral Science Foundation (Nos. 2024T170557 and 2023M742224), Shanghai Postdoctoral Excellence Program (No. 2023440), the National Natural Science Foundation of China (No. 52401101), and City University of Hong Kong Donation Research Grants (9220061 and DON-RMG 9229021).

Appendix A. Supporting information

Supplementary data associated with this article can be found in the online version at doi:10.1016/j.corsci.2025.113116.

Data availability

Data will be made available on request.

References

[1] J. Chen, X. Zhou, W. Wang, B. Liu, Y. Lv, W. Yang, D. Xu, Y. Liu, A review on fundamental of high entropy alloys with promising high–temperature properties, J. Alloy. Compd. 760 (2018) 15–30.
[2] L. Li, J. Lu, X. Liu, T. Dong, X. Zhao, F. Yang, F. Guo, Al_xCoCrFeNi high entropy alloys with superior hot corrosion resistance to Na_2SO_4 + 25% NaCl at 900 °C, Corros. Sci. 187 (2021) 1–14.
[3] W.-L. Hsu, C.-W. Tsai, A.-C. Yeh, J.-W. Yeh, Clarifying the four core effects of high-entropy materials, Nat. Rev. Chem. 8 (2024) 471–485.
[4] W.X. Wu, H.X. Liu, X.M. Jin, L.L. Guo, T. Zhu, L.B. Hu, C. Yang, P.H. Chen, C.J. Qiu, P.K. Chu, Unveiling high-temperature tribological behavior and wear mechanism of WCp/HEA composite coating via laser additive manufacturing, Ceram. Int. 51 (2025) 19485–19496.
[5] D.B. Miracle, O.N. Senkov, A critical review of high entropy alloys and related concepts, Acta Mater. 122 (2017) 448–511.
[6] P. Edalati, A. Mohammadi, Y. Tang, R. Floriano, M. Fuji, K. Edalati, Phase transformation and microstructure evolution in ultrahard carbon-doped AlTiFeCoNi high-entropy alloy by high-pressure torsion, Mater. Lett. 302 (2021) 130368.
[7] P. Edalati, A. Mohammadi, M. Ketabchi, K. Edalati, Ultrahigh hardness in nanostructured dual-phase high-entropy alloy AlCrFeCoNiNb developed by high-pressure torsion, J. Alloy. Compd. 884 (2021) 161101.
[8] P. Edalati, A. Cremasco, K. Edalati, R. Floriano, High corrosion resistance of nanograined and nanotwinned Al0.1CoCrFeNi high-entropy alloy processed by high-pressure torsion, Intermetallics 172 (2024) 108368.
[9] Y. Lu, Y. Dong, S. Guo, L. Jiang, H. Kang, T. Wang, B. Wen, Z. Wang, J. Jie, Z. Cao, H. Ruan, T. Li, A promising new class of high-temperature alloys: eutectic high-entropy alloys, Sci. Rep. 4 (2014) 6200.
[10] M.E. Glicksman. Principles of Solidification: an Introduction to Modern Casting and Crystal Growth Concepts, Springer Science & Business Media, 2010.
[11] Y. Lu, X. Gao, L. Jiang, Z. Chen, T. Wang, J. Jie, H. Kang, Y. Zhang, S. Guo, H. Ruan, Y. Zhao, Z. Cao, T. Li, Directly cast bulk eutectic and near-eutectic high entropy alloys with balanced strength and ductility in a wide temperature range, Acta Mater. 124 (2017) 143–150.
[12] Y. Lu, Y. Dong, H. Jiang, Z. Wang, Z. Cao, S. Guo, T. Wang, T. Li, P.K. Liaw, Promising properties and future trend of eutectic high entropy alloys, Scr. Mater. 187 (2020) 202–209.
[13] C.S. Tiwary, P. Pandey, S. Sarkar, R. Das, S. Samal, K. Biswas, K. Chattopadhyay, Five decades of research on the development of eutectic as engineering materials, Prog. Mater. Sci. 123 (2022) 100793.
[14] C.S. Tiwary, S. Kashyap, K. Chattopadhyay, Development of alloys with high strength at elevated temperatures by tuning the bimodal microstructure in the Al-Cu-Ni eutectic system, Scr. Mater. 93 (2014) 20–23.
[15] Z. Peng, J. Sun, H. Luan, N. Chen, K. Yao, Effect of Mo on the high temperature oxidation behavior of $Al_{19}Fe_{20-x}Co_{20-x}Ni_{41}Mo_{2x}$ high entropy alloys, Intermetallics 155 (2023) 107845.
[16] D. Mondal, J. Das, Enhanced oxidation resistance in nano-lamellar $CoCrFeNiNb_x$ ($0.45 \leq x \leq 0.55$) eutectic high entropy alloy during cyclic oxidation at 700-1100 °C, Corros. Sci. 240 (2024) 112497.
[17] Z. Dong, A. Sun, S. Yang, X. Yu, H. Yuan, Z. Wang, L. Deng, J. Song, D. Wang, Y. Kang, Machine learning-assisted discovery of Cr, Al-containing high-entropy alloys for high oxidation resistance, Corros. Sci. 220 (2023) 111222.
[18] K.-C. Lo, Y.-J. Chang, H. Murakami, J.-W. Yeh, A.-C. Yeh, An oxidation resistant refractory high entropy alloy protected by $CrTaO_4$-based oxide, Sci. Rep. 9 (2019) 7266.
[19] P. Kumar, T.N. Lam, P.K. Tripathi, S.S. Singh, P.K. Liaw, E.W. Huang, Recent progress in oxidation behavior of high-entropy alloys: A review, APL Mater. 10 (2022) 120701, https://doi.org/10.1063/5.0116605.
[20] S. Kumar T, A. Sourav, S. Yebaji, L. Chauhan, A. Babu, A. Chelvane, T. Shanmugasundaram, Effect of heat treatment on the oxidation behavior of an $AlCoCrFeNi_2$ near-eutectic high entropy alloy, Corros. Sci. 221 (2023) 111298.
[21] G. Lin, Z. Cai, Y. Dong, C. Wang, J. Hu, P. Zhang, L. Gu, High-temperature oxidation behavior of $AlCoCrFeNi_{2.1}$ eutectic high-entropy alloy: microstructure evolution and microhardness, Mater. Charact. 210 (2024) 1–9.
[22] N. Yurchenko, E. Panina, S. Zherebtsov, N. Stepanov, Oxidation behaviour of eutectic refractory high-entropy alloys at 800-1000 °C, Corros. Sci. 205 (2022) 110464.
[23] L. Han, T. Quan, B. Liu, X. Xu, Y. Liu, Revealing the excellent high-temperature oxidation resistance of a non-equimolar $Al_1Co_{25}Cr_{18}Fe_{23}Ni_{23}Ta_{10}$ compositional complex eutectic alloy, J. Alloy. Compd. 846 (2020) 156265.
[24] J. Lu, H. Zhang, Y. Chen, L. Ling, X. Liu, W. Xiao, N. Ni, X. Zhao, F. Guo, P. Xiao, Y-doped $AlCoCrFeNi_{2.1}$ eutectic high-entropy alloy with excellent oxidation resistance and structure stability at 1000 °C and 1100 °C, Corros. Sci. 180 (2021) 109191.
[25] A. Huang, L. Li, X. Liu, H. Zhang, M. Li, X. Zhang, J. Lu, X. Zhao, Superior oxidation resistance of a Y-Hf co-doped $Al_{18}Co_{30}Cr_{10}Fe_{10}Ni_{32}$ eutectic high-entropy alloy at 1100-1300 °C, J. Alloy. Compd. 992 (2024) 174597.
[26] J. Lu, H. Zhang, L. Li, Y. Chen, X. Liu, X. Zhao, F. Guo, Y-Hf co-doped $AlCoCrFeNi_{2.1}$ eutectic high-entropy alloy with excellent oxidation and spallation resistance under thermal cycling conditions at 1100 °C and 1200 °C, Corros. Sci. 187 (2021) 109515.
[27] J. Lu, H. Zhang, G. Ren, Y. Chen, L. Luo, H. Cai, X. Shan, X. Zhang, X. Zhao, A comparative study on the oxidation behavior and failure mechanisms of conventional NiCoCrAl alloy and in-situ composite $AlCoCrFeNi_{2.1}$ eutectic high-entropy alloy at 1300 °, C. Compos. Part B 269 (2023) 111097.
[28] J.L. Smialek, Invited review paper in commemoration of Over 50 years of oxidation of metals: alumina scale adhesion mechanisms: a retrospective assessment, Oxid. Met. 97 (2022) 1–50.
[29] B.A. Pint, Optimization of reactive-element additions to improve oxidation performance of alumina-forming alloys, J. Am. Ceram. Soc. 86 (2003) 686–695.
[30] J. Wang, J. Wang, B. Wu, L. Wang, Z. Long, X. Yu, L. Hou, X. Fan, B. Sun, X. Li, Excellent strength-ductility synergy assisted by dislocation dipole-induced plasticity in Co-free precipitate-strengthened medium-entropy alloy, Int. J. Plast. 181 (2024) 104109.
[31] Y.L. Zhao, T. Yang, J.H. Zhu, D. Chen, Y. Yang, A. Hu, C.T. Liu, J.J. Kai, Development of high-strength Co-free high-entropy alloys hardened by nanosized precipitates, Scr. Mater. 148 (2018) 51–55.
[32] S. Hayashi, Y. Takada, S. Yoneda, S. Ukai, Metastable-stable phase transformation behavior of Al_2O_3 scale formed on Fe–Ni–Al alloys, Oxid. Met. 86 (2016) 151–164.
[33] W. Chen, X. Shan, J. Li, Y. Guo, F. Guo, X. Zhao, N. Ni, P. Xiao, Effects of iron and platinum on the isothermal oxidation of β-NiAl overlay coatings fabricated by spark plasma sintering, Surf. Coat. Technol. 382 (2020) 125178.
[34] X. Jin, J. Bi, L. Zhang, Y. Zhou, X. Du, Y. Liang, B. Li, A new $CrFeNi_2Al$ eutectic high entropy alloy system with excellent mechanical properties, J. Alloy. Compd. 770 (2019) 655–661.
[35] R.J. Christensen, V.K. Tolpygo, D.R. Clarke, The influence of the reactive element yttrium on the stress in alumina scales formed by oxidation, Acta Mater. 45 (1997) 1761–1766.
[36] B.A. Pint, Experimental observations in support of the dynamic-segregation theory to explain the reactive-element effect, Oxid. Met. 45 (1996) 1–37.
[37] E.W.A. Young, J.H.W. Dewit, An ^{18}O tracer study on the growth mechanism of alumina scales on NiAl and NiAlY alloys, Oxid. Met. 26 (1986) 351–361.
[38] D.J. Young. High Temperature Oxidation and Corrosion of Metals, Elsevier, 2008.
[39] C. Wagner, Theoretical analysis of the diffusion processes determining the oxidation rate of alloys, J. Electrochem. Soc. 99 (1952) 369–380.
[40] H.E. Evans, M.P. Taylor, Diffusion cells and chemical failure of MCrAlY bond coats in thermal-barrier coating systems, Oxid. Met. 55 (2001) 17–34.
[41] F. Ebrahimi, S. Shrivastava, Brittle-to-ductile transition in NiAl single crystal, Acta Mater. 46 (1998) 1493–1502.
[42] P.Y. Hou, K. Priimak, Interfacial segregation, pore formation, and scale adhesion on NiAl alloys, Oxid. Met. 63 (2005) 113–130.
[43] C. Zhu, X. Zhao, Y. Chen, Y. Zhao, P. Xiao, I.S. Molchan, G.E. Thompson, Spallation behaviour of alumina scale formed on FeCrAlY alloy after isothermal oxidation, Oxid. Met. 85 (2016) 391–408.
[44] L. Li, Y. Chen, A. Huang, X. Liu, H. Zhang, H. Zhang, X. Zhang, J. Lu, X. Zhao, A novel NiCoCrAlPt high-entropy alloy with superb oxidation resistance at 1200 °C, Corros. Sci. 228 (2024) 111819.
[45] A. Huang, Y. Chen, Z. Zhang, J. Shen, L. Li, X. Liu, H. Zhang, J. Lu, X. Zhao, Effect of Al content on the oxidation behavior of NiCoCrAlYHf alloys at 1100 °C, Corros. Sci. 222 (2023) 111417.
[46] B.A. Pint, K.L. More, I.G. Wright, Effect of quaternary additions on the oxidation behavior of Hf-doped NiAl, Oxid. Met. 59 (2003) 257–283.
[47] C. Yang, T. Ying, A.H. Huang, J. Huang, P.H. Chen, P.K. Chu, X.Q. Zeng, Enhancing the corrosion resistance of MAO coatings on LY12 alloy by in situ co-doping with zinc phosphate and cerium phosphate, Corros. Commun. 17 (2025) 35–43.
[48] M.W. Brumm, H.J. Grabke, The oxidation behaviour of NiAl-I. Phase transformations in the alumina scale during oxidation of NiAl and NiAl-Cr alloys, Corros. Sci. 33 (1992) 1677–1690.
[49] H. Yu, S. Kondo, R. Kasada, S. Ukai, Influence of Ni content on the oxidation behavior of alumina-forming Co-based oxide dispersion strengthened superalloys at 900 °C, Corros. Sci. 212 (2023) 1–14.
[50] Y. Chen, X. Zhao, P. Xiao, Effect of microstructure on early oxidation of MCrAlY coatings, Acta Mater. 159 (2018) 150–162.
[51] H. Zhou, Y. Ji, Y. Wang, K. Feng, B. Luan, X. Zhang, L.-Q. Chen, First-principles lattice dynamics and thermodynamic properties of α-, θ-, κ- and γ-Al_2O_3 and solid state temperature-pressure phase diagram, Acta Mater. 263 (2024) 119513.

[52] V.K. Tolpygo, J.R. Dryden, D.R. Clarke, Determination of the growth stress and strain in α-Al_2O_3 scales during the oxidation of Fe-22Cr-4.8Al-0.3Y alloy, Acta Mater. 46 (1998) 927–937.
[53] H. Yu, R. Kasada, K. Inoue, S. Kondo, Y. Ogino, S. Ukai, Contribution of Y_2O_3/Hf co-doping to alumina scale growth on oxide dispersion strengthened Co-based superalloy, Corros. Sci. 227 (2024) 111775.
[54] R. Raggio, G. Borzone, R. Ferro, The Al-rich region in the Y–Ni–Al system: microstructures and phase equilibria, Intermetallics 8 (2000) 247–257.
[55] J. Huang, B. Yang, H. Chen, H. Wang, Thermodynamic optimisation of the Ni-Al-Y ternary system, J. Phase Equilibria Diffus 36 (2015) 357–365.
[56] L. Qiu, F. Yang, W. Zhang, X. Zhao, P. Xiao, Effect of Al content on the lifetime of thermally grown oxide formed on Ni-Al alloys after isothermal oxidation, Corros. Sci. 89 (2014) 13–20.
[57] J.A. Haynes, B.A. Pint, W.D. Porter, I.G. Wright, Comparison of thermal expansion and oxidation behavior of various high-temperature coating materials and superalloys, Mater. High Temp. 21 (2004) 87–94.
[58] S. Gorsse, M.H. Nguyen, O.N. Senkov, D.B. Miracle, Database on the mechanical properties of high entropy alloys and complex concentrated alloys, Data Br. 21 (2018) 2664–2678.
[59] Y. Ikeda, F. Körmann, I. Tanaka, J. Neugebauer, Impact of chemical fluctuations on stacking fault energies of CrCoNi and CrMnFeCoNi high entropy alloys from first principles, Entropy 20 (2018), https://doi.org/10.3390/e20090655.
[60] A.H. Huang, C. Yang, X.Z. Liu, H. Zhang, F.W. Guo, B.N. Qian, J. Lu, X.F. Zhao, P. K. Chu, Oxidation behavior and failure mechanism of NiCoCrAl eutectic multi-principal element alloys co-doped with Y and Hf at 1100 ℃ and 1200 ℃, Corros. Sci. 253 (2025) 112944.

Supplementary material

Temperature-dependent oxidation behavior of Y-Hf co-doped and Co-free $Al_{16}Cr_{20}Fe_{20}Ni_{44}$ eutectic multi-principal elements alloy at 1100-1300 °C

Aihui Huang [a, b], Yusheng Tian [a, b], Yifeng Tang [a, b], Guoliang Zhu [a, b *], Shilin Xia[a], Xiaofeng Zhao [b], Paul K. Chu [d], Chao Yang [c*], Xiaoqin Zeng [c]

[a] Suzhou Laboratory, Suzhou, 215000, China

[b] Shanghai Key Laboratory of Advanced High-Temperature Materials and Precision Forming, School of Materials Science and Engineering, Shanghai Jiao Tong University, Shanghai, 200240, China

[c] National Engineering Research Center of Light Alloy Net Forming, Shanghai Jiao Tong University, Shanghai, 200240, China

[d] Department of Physics, Department of Materials Science & Engineering, and Department of Biomedical Engineering, City University of Hong Kong, Tat Chee Avenue, Kowloon, Hong Kong 999077, China

[*] Corresponding authors: Chao Yang (chaoyang0315@163.com); Guoliang Zhu (glzhu@sjtu.edu.cn)

Section 1 XPS analysis of Y-Hf co-doped and Co-free $Al_{16}Cr_{20}Fe_{20}Ni_{44}$ eutectic multi-principal elements alloy after oxidation at 1100-1200 ℃.

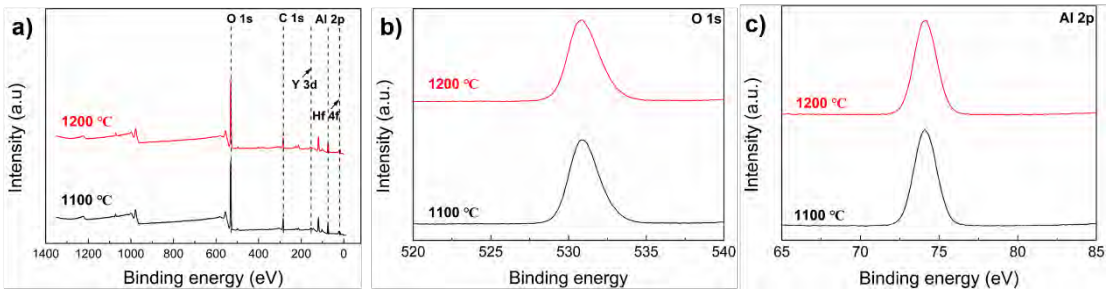

Fig. S1 XPS analysis of Y-Hf co-doped Y-Hf co-doped $Al_{16}Cr_{20}Fe_{20}Ni_{44}$ EMPEA after 500 h oxidation at 1100℃ and 1200 ℃: (a) Total spectra; (b) O 1s spectra; (c) Al 2p spectra.

Table S1 Atomic percent of Y-Hf co-doped Y-Hf co-doped $Al_{16}Cr_{20}Fe_{20}Ni_{44}$ EMPEA after 500 h oxidation at 1100 ℃ and 1200 ℃ determined by XPS analysis.

Photoelectron peak	At.% (1100 ℃ 500 h)	At.% (1200 ℃ 500 h)
C 1s	25.98	24.44
O 1s	45.96	46.88
Al 2p	27.37	27.40
Hf 4f	0.49	0.87
Y 3d	0.20	0.41

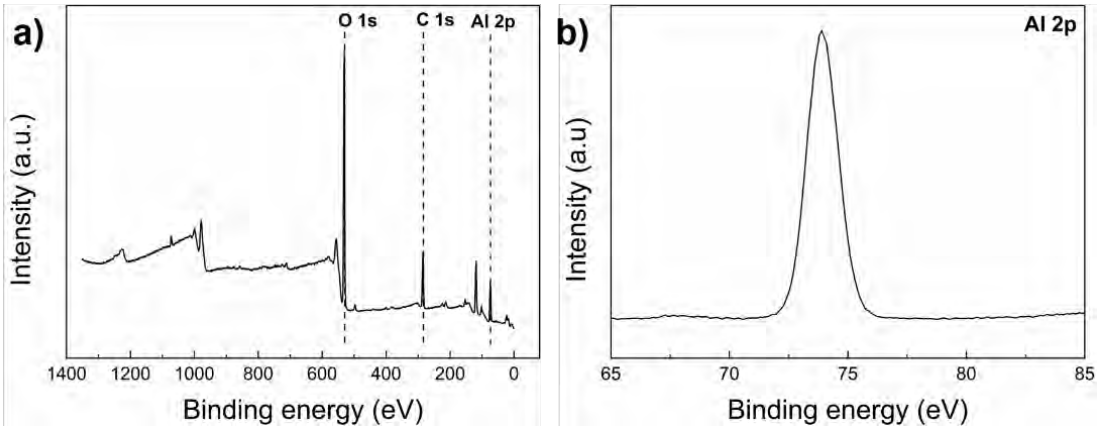

Fig. S2 XPS analysis of Y-Hf co-doped Y-Hf co-doped $Al_{16}Cr_{20}Fe_{20}Ni_{44}$ EMPEA after 5 minutes oxidation at 1100 ℃: (a) Total spectra; (b) Al 2p spectra.

Section 2 TEM analysis of RE distribution on the Y-Hf co-doped $Al_{16}Cr_{20}Fe_{20}Ni_{44}$ EMPEA

After 500 hours oxidation at 1100 °C for 500 hours, discrete subscale precipitates were observed in the oxidized sample. To further investigate these features, we conducted FIB sample preparation followed by TEM analysis. As shown in **Fig. S3a-c**, STEM-HADDF imaging and corresponding EDS mapping reveal the presence of RE-rich precipitates with sizes around 1 μm, enriched in both Y, Al and Hf (Al: 32.3 at.%, Hf: 64.6 at.%, Y: 3.1 at.%), which seemed to be the Hf_2Al compound. These precipitates are located in the substrate, indicating localized segregation rather than internal oxidation. Moreover, as shown in **Fig. S3d-f**, additional high-resolution STEM-HADDF and EDS mapping demonstrate that Hf is also preferentially distributed at β phase, suggesting a strong tendency for Hf segregation. These findings confirm the accuracy of our thermal-calc calculation.

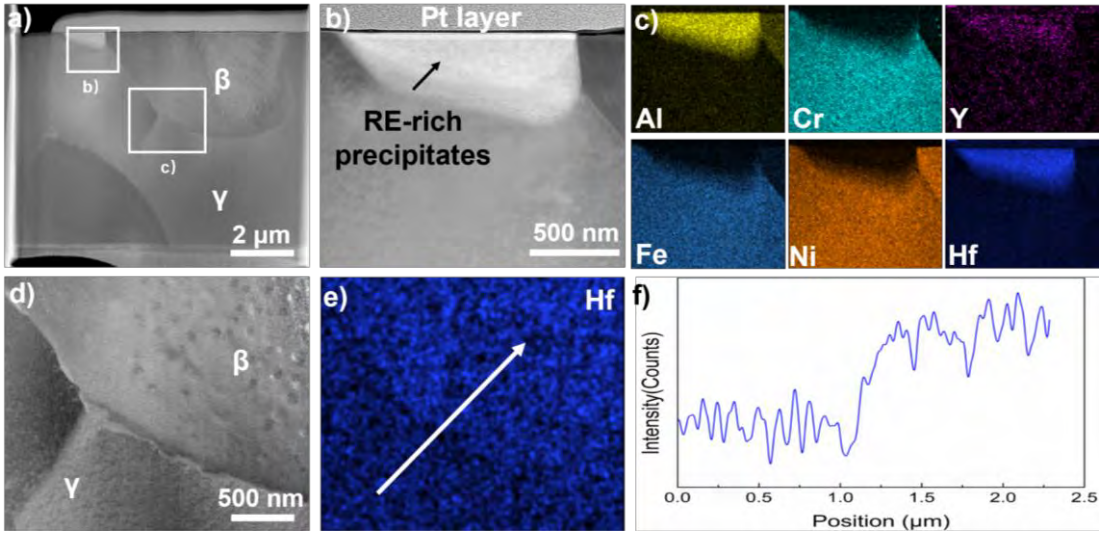

Fig. S3 TEM analysis of RE distribution on the Y-Hf co-doped $Al_{16}Cr_{20}Fe_{20}Ni_{44}$ EMPEAs after 500 h oxidation at 1100 ℃: (a) Low magnification STEM-HADDF image, showing the overview of the FIB-processed sample; (b-c) High magnification STEM-HADDF image and corresponding EDS mapping, showing the detail and elemental distribution of RE-rich precipitates; (d-f) High magnification STEM-HADDF image and corresponding EDS mapping of Hf, showing the distribution of Hf on the γ and β phase.

Section 3 Mass gain curves of Y-Hf co-doped $Al_{16}Cr_{20}Fe_{20}Ni_{44}$ EMPEA after high temperature oxidation at 1100-1200 ℃

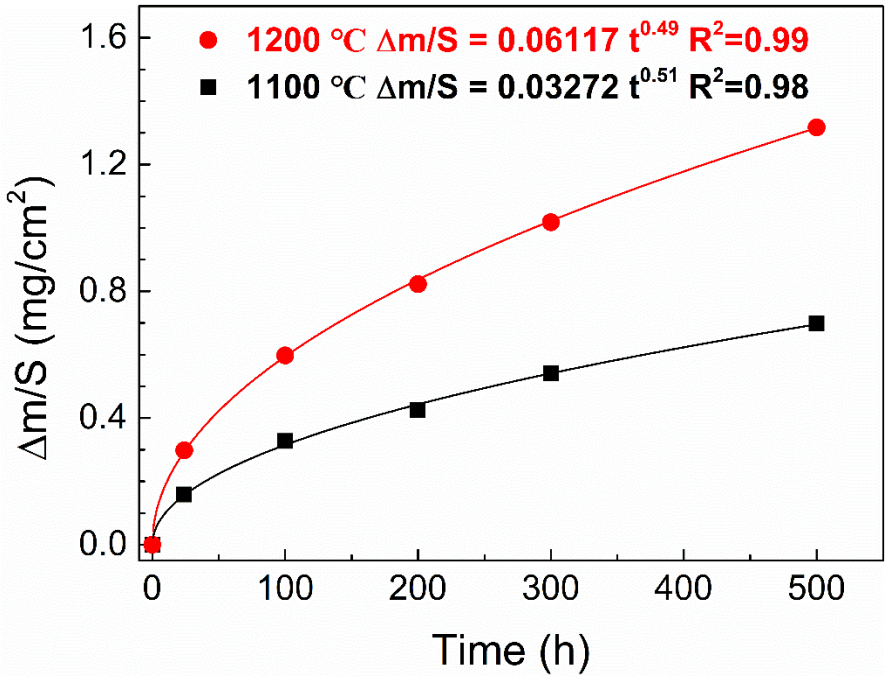

Fig. S4 Δm/S kinetic curves of the Y-Hf co-doped $Al_{16}Cr_{20}Fe_{20}Ni_{44}$ EMPEA after high temperature oxidation at 1100-1200 ℃ fitted with power equation.

Section 4 High temperature compressive properties of Y-Hf co-doped $Al_{16}Cr_{20}Fe_{20}Ni_{44}$ and $Al_{18}Co_{20}Cr_{20}Ni_{42}$ EMPEAs at 1300 ℃.

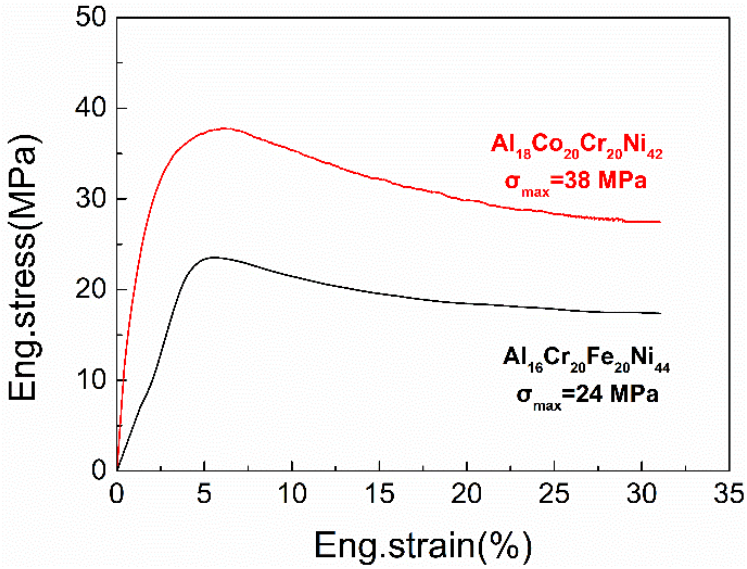

Fig. S5 High temperature compressive curves of Y-Hf co-doped $Al_{16}Cr_{20}Fe_{20}Ni_{44}$ and $Al_{18}Co_{20}Cr_{20}Ni_{42}$ EMPEAs at 1300 ℃.

Section 5 EBSD analysis of Y-Hf co-doped $Al_{16}Cr_{20}Fe_{20}Ni_{44}$ EMPEA after 500 h oxidation at 1200 ℃.

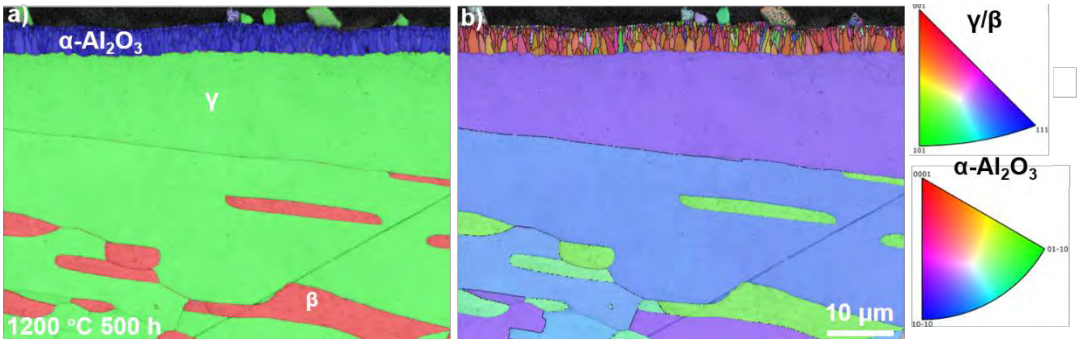

Fig. S6 EBSD analysis of Y-Hf co-doped $Al_{16}Cr_{20}Fe_{20}Ni_{44}$ EMPEA after 500 h oxidation at 1200 ℃: (a) Phase map, showing the distribution of different phases; (b) IPF map, illustrating the crystal orientations of these phases.